Ocean Engineering 38 (2011) 579–591

Contents lists available at ScienceDirect

Ocean Engineering

journal homepage: www.elsevier.com/locate/oceaneng

Propagation of water waves over permeable rippled beds

Ching-Jer Huang*, Chih-Hsin Chen, Hsing-Han Chang

Department of Hydraulic and Ocean Engineering, National Cheng Kung University, Tainan, Taiwan 701

ARTICLE INFO

Article history:
Received 23 September 2009
Accepted 6 December 2010
Editor-in-Chief: A.I. Incecik
Available online 21 December 2010

Keywords:
Water waves
Permeable rippled bed
Navier–Stokes equations
Streaming velocity
Particle trajectories

ABSTRACT

Unsteady two-dimensional Navier–Stokes equations and Navier–Stokes type model equations for porous flow were solved numerically to simulate the propagation of water waves over a permeable rippled bed. A boundary-fitted coordinate system was adopted to make the computational meshes consistent with the rippled bed. The accuracy of the numerical scheme was confirmed by comparing the numerical results concerning the spatial distribution of wave amplitudes over impermeable and permeable rippled beds with the analytical solutions. For periodic incident waves, the flow field over the wavy wall is discussed in terms of the steady Eulerian streaming velocity. The trajectories of the fluid particles that are initially located close to the ripples were also determined. One of the main results herein is that under the action of periodic water waves, fluid particles on an impermeable rippled bed initially moved back and forth around the ripple crest, with increasing vertical distance from the rippled wall. After one or two wave periods, they are then lifted towards the next ripple crest. All of the marked particles on a permeable rippled bed were shifted onshore with a much larger displacement than those on an impermeable bed. Finally, the flow fields and the particle motions close to impermeable and permeable beds induced by a solitary wave are elucidated.

1. Introduction

Several studies have examined the propagation of water waves over rippled beds to elucidate the transport mechanism of sediment on erodible beds. Laboratory experiments on oscillating flows over ripples have revealed that two stationary cells are always present between ripple crests (Horikawa and Watanabe, 1968; Johnson and Carlsen, 1976). Laser Doppler velocimetry has also been used to measure the flow fields near the crest and trough section of wavy walls (Sato et al., 1987; Ranasoma and Sleath, 1992). The flows above the ripples are commonly turbulent. The characteristics of the turbulent flows close to the ripples have been discussed in terms of eddy viscosity, and the production and dissipation rates of the turbulent energy in the boundary layer close to the wall, and the relationship between these properties and vortex formation has been considered.

Lyne (1971) was the first to study theoretically oscillating flows over a rippled bottom. The important physical parameters in this problem are the frequency ω and the amplitude A of the oscillatory flow, the ripple amplitude a_s, the ripple wavelength λ_s (wavenumber $k_s=2\pi/\lambda_s$), and the fluid viscosity υ. Hara and Mei (1990a) indicated that these parameters could be used to determine three dimensionless numbers, the ripple slope $\varepsilon=k_sa_s$, the Keulegan–Carpenter number $\alpha=k_sA$ and the viscous diffusion parameter $\sigma=k_s\delta$, where $\delta=\sqrt{\nu/\omega}$ is the characteristic thickness of the boundary layer. Analytical solutions for different values of ε and α were obtained by Hara and Mei (1990b), Blondeaux (1990) and Blondeaux and Vittori (1991).

Davies and Villaret (1999) proposed an analytical model to predict the Eulerian drift that is caused by progressive waves over rippled, or very rough beds. The behavior of this drift differs markedly from that predicted by Longuet-Higgins (1953) for a flat bed. Ridler and Sleath (2000) made measurements to study the Eulerian time-mean drift that is induced by progressive water waves over rough beds. They observed that within certain ranges of parameters, near-bed mean drift was in the direction opposite to that of the wave propagation. Marin (2004) performed laboratory experiments to compare the experimental Eulerian drifts with the analytical drifts that were obtained by Davies and Villaret (1999) and Longuet-Higgins (1953).

The resonant Bragg scattering of surface waves over wavy walls has also attracted much attention as one of the mechanisms for the development of multiple shore-parallel bars. Since resonant Bragg scattering causes the strong reflection of incident water waves, artificial periodic bars can be employed as a wave control system. Davies and Heathershaw (1984) studied reflection from a sinusoidal undulation over a horizontal bottom and evaluated the reflection coefficient. Their experimental results indicated a resonant Bragg reflection when the wavelength of the bottom undulation was half of the wavelength of the surface wave, as was predicted by their theory. Kirby (1986) derived a general wave equation by extending the mild slope equation of Berkhoff (1972) to analyze the transformation of waves that propagate over a rippled bed.

* Corresponding author. Tel.: +886 6 2757575x63252.
E-mail addresses: cjhuang@mail.ncku.edu.tw (C.-J. Huang), n8892111@mail.ncku.edu.tw (C.-H. Chen), n8886101@ms26.hinet.net (H.-H. Chang).

0029-8018/$ - see front matter © 2010 Elsevier Ltd. All rights reserved.
doi:10.1016/j.oceaneng.2010.12.003

Huang and Dong (2002) solved numerically the unsteady, two-dimensional Navier–Stokes equations with exact free surface boundary conditions to simulate the propagation of water waves over impermeable rippled beds. Based on their results, the propagation of a solitary wave above a rigid rippled bed produces a near-bed current in the direction opposite to that of the wave. This effect differs from that associated with periodic waves. Barr et al. (2004) examined turbulent oscillatory flow over sand ripples by using three-dimensional numerical simulations. They found that the presence of sand ripples increases the dissipation rate of the shoaling wave energy above that associated with flow over smooth boundary. Malarkey and Davies (2004) proposed a formula for eddy viscosity for oscillatory flow over vortex ripples, based on the results for ripples of various shapes and steepness, determined using a discrete vortex model.

Previous works have assumed that the rippled bed is impermeable and that an equilibrium configuration has been reached, such that the gravitational force that acts on the sedimentary particles balances the drag associated with the motion of the fluid. Martin (1970) performed laboratory experiments to elucidate the effect of a porous sand bed on the incipient motion of sediment. He reported that seepage may either enhance or hinder incipient motion, depending on the relative magnitude of the boundary layer stress and the seepage stress. Mase et al. (1995) extended Kirby's theory (1986) to derive a time-dependent wave equation for waves that propagate over permeable rippled beds. The unsteady motion of the fluid in the porous bed was determined by the equation of Sollitt and Cross (1972). They found that the permeability of the rippled bed makes the amplitude of transmitted waves small. The friction factor, the thickness of the porous layer, and the porosity all affect the reflection and transmission coefficients. Silva et al. (2002) used an approach similar to that presented by Chamberlain and Porter (1995) to obtain a new modified mild slope equation for the interaction of waves with a submerged porous structure. Their model was validated by comparing their results for the spatial distribution of wave height above a rippled porous bed with the analytical results of Mase et al. (1995). The results of Mase et al. (1995) are also used herein to confirm the accuracy of the proposed numerical model. Hsiao and Liu (2003) investigated the viscous boundary layer flows above and within a permeable wavy bed that are induced by an oscillatory horizontal flow. They noted that permeability significantly altered the steady streaming pattern, such that this pattern changes from having two pairs of recirculating cells in the inner and outer layers above an impervious wavy bed to just a pair of recirculating cells above a permeable bed.

A review of the literature reveals that the propagation of water waves over permeable rippled beds has seldom been investigated. The effects of the porosity and permeability on the flow field and the particle motion near an undulating bottom remain to be determined. Such a determination depends on appropriate governing equations for the porous flows and suitable boundary conditions around the permeable rippled bed.

Although the porous flow model of Sollitt and Cross (1972) has been extensively used to study the interaction of water waves and porous structures, several have recently proposed Navier–Stokes type models. They include van Gent (1995), Liu et al. (1999), and Huang et al. (2003). Compared to the previous models, the Navier–Stokes type models retain both the convective inertial force term and the viscous force term. The convection term captures the nonlinear effect for the wave structure interaction, while the viscous term completes the forces on the pore flow. The model of Huang et al. (2003) differs from that of van Gent (1995) and Liu et al. (1999) in that it maintains the inertial coefficient and the laminar and turbulent resistance coefficients of Sollitt and Cross (1972). The model of Liu et al. (1999) has been used and further modified by some authors (Hsu et al., 2002; Lara et al., 2006; Losada et al., 2008; Cheng et al., 2009, among many others). Similarly, Huang et al. (2008) and Shao (2010) used the model of Huang et al. (2003) to elucidate the interactions of waves with porous structures.

The present work develops a numerical model to investigate the interaction of free surface waves and a porous rippled bed whose ripples have a wavelength that is significantly smaller than the wavelength of incident waves. This rippled bed represents sea ripples rather than shore-parallel bars, whose size is usually comparable with the wavelength of sea waves. The Navier–Stokes equations and the Navier–Stokes type model equations proposed by Huang et al. (2003) for porous flows were solved numerically to determine the flows in the water region and in the porous rippled bed, respectively. The accuracy of the numerical approach was verified by comparing the numerical results for the spatial distribution of wave heights on the impermeable and permeable rippled beds with the analytical solutions of Mase et al. (1995). The characteristics of the flow fields near the rippled bed that are induced by periodic waves and solitary waves were discussed. The trajectories of the fluid particles with initial locations close to the ripples were also determined.

Since the model that is proposed in this work solves the viscous flow equations under the complete boundary conditions at the free surface and the interfaces, the model is extensively applicable for predicting both the wave and flow fields associated with the propagation of waves over submerged porous structures. The assumption of laminar flow regimes in the water region can be eliminated if, instead of the Navier–Stokes equations, the Reynolds Averaged Navier–Stokes (RANS) equations are solved, and a suitable turbulent flow model, such as the k–ε model, is adopted. This work demonstrates the application of this model to examine the interaction of water waves with a porous wavy wall using a body-fitted coordinate system.

2. Governing equations and boundary conditions

This work studies the propagation of water waves over rippled beds. The rippled bed can be impermeable or permeable. Fig. 1 schematically depicts the rippled bed at the bottom of a two-dimensional numerical wave tank. A piston-type wavemaker with stroke S_o is located at $x=0$ and generates incident periodic and solitary waves. The still water depth is h_o. When the rippled bed is permeable, the porosity, n_w, and the intrinsic permeability, K_p(with dimension L^2, where L is length), are assumed to be homogeneous. The flow outside the rippled bed is assumed to be laminar and determined by solving unsteady two-dimensional Navier–Stokes equations. The pore flow in the permeable rippled bed is described

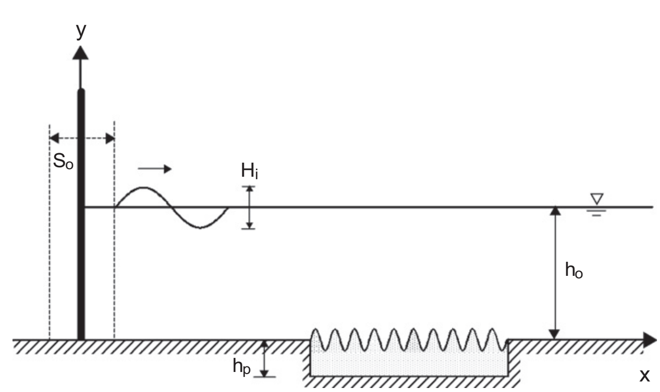

Fig. 1. Schematic diagram of water waves propagating over impermeable or permeable rippled bed.

by the dimensionless Navier–Stokes type equations (Huang et al., 2003)

$$\frac{\partial u}{\partial x}+\frac{\partial v}{\partial y}=0 \tag{1}$$

$$S\frac{\partial u}{\partial t}+u\frac{\partial u}{\partial x}+v\frac{\partial u}{\partial y}=-\frac{\partial p}{\partial x}+\frac{1}{\mathrm{Re}}\left(\frac{\partial^2 u}{\partial x^2}+\frac{\partial^2 u}{\partial y^2}\right)-Ku-K_f u\sqrt{u^2+v^2} \tag{2}$$

$$S\frac{\partial v}{\partial t}+u\frac{\partial v}{\partial x}+v\frac{\partial v}{\partial y}=-\frac{\partial p}{\partial y}+\frac{1}{\mathrm{Re}}\left(\frac{\partial^2 v}{\partial x^2}+\frac{\partial^2 v}{\partial y^2}\right)-Kv-K_f v\sqrt{u^2+v^2} \tag{3}$$

where u and v are the horizontal and vertical velocity components in the Cartesian coordinates (x,y); t is time; p represents hydrodynamic pressure; $S=1+(1-n_w)C_m/n_w$ is the inertial coefficient, and C_m is the coefficient of added mass. The velocity in the above equations is the discharge velocity, which equals the Darcian velocity divided by the porosity; it is physically interpreted as a spatially averaged quantity. In Eqs. (1)–(3), the velocity and length are non-dimensionalized using u_o and h_o, where $u_o=cH_i/h_o$; c is the phase speed, and H_i is the incident wave height. Time is non-dimensionalized using $t_o=u_o/h_o$. The pressure is non-dimensionalized using ρu_o^2, where ρ is the density of the fluid. The Reynolds number Re, and the dimensionless parameters K and K_f are defined as

$$\mathrm{Re}=u_o h_o/\upsilon,\ K=\upsilon n_w h_o/K_P u_o \ \text{ and }\ K_f=C_f n_w^2 h_o/\sqrt{K_P} \tag{4}$$

where υ is the kinematic viscosity of the fluid and C_f is a dimensionless turbulent resistance coefficient.

To solve Eqs. (2) and (3), the permeability coefficient K_p, the nonlinear resistance force C_f, and the inertial coefficient S, must be determined. According to McDougal (1993), if the porosity and the grain size d of the porous structure are known, then K_p can be determined as follows:

$$K_p=1.643\times 10^{-7}\left[\frac{d(\mathrm{mm})}{d_o}\right]^{1.57}\frac{n_w^3}{(1-n_w)^2},\ d_o=10\,\mathrm{mm} \tag{5}$$

According to Arbhabhiramar and Dinoy (1973),

$$C_f=100\left[d(m)\left(\frac{n_w}{K_p}\right)^{1/2}\right]^{-1.5} \tag{6}$$

The inertial coefficient S must be determined experimentally. It is commonly taken as one in analysis. In this study, S was taken as unity. Notably, the mechanical properties of the porous flow depend on not only the permeability and the porosity, but also the inertia coefficient, S. Therefore, to determine in detail the effects of the porous structure on porous flows, attention must also be paid to the effect of S. Van Gent (1995) offered a good explanation of the range of the inertial coefficients obtained in oscillating flow tests.

To make the computational meshes consistent with the rippled beds, the proposed model adopts a boundary-fitted coordinate system. The curvilinear grid system is generated using the algebraic coordinate method (Thompson et al., 1985). The physical domain (x,y) is transformed into the computational domain (ξ,η). To transform the equations of motion from the familiar orthogonal coordinates (x,y), to the new coordinate system (ξ,η), a partial transformation was used, meaning that only the independent coordinate variables were transformed, leaving the dependent variables (the velocity components) in the original orthogonal coordinates. Therefore, the variables are transformed from physical space (x,y,t) into computational space (ξ,η,t). Huang and Dong (2002) presented the transformed forms of the continuity equation and the Navier–Stokes equations. Eqs. (2) and (3) differ from the Navier–Stokes equations only in that they contain additional porous flow terms.

To solve the Navier–Stokes equations for the motion of water above the bed, the boundary conditions at all of the boundaries of the solution domain must be provided, and initial conditions set throughout the domain. The fully-nonlinear kinematic and dynamic boundary conditions at the free surface are satisfied (Huang et al., 1998). Dong and Huang (2004) provided details concerning the accuracy of the numerical wave and velocity profiles obtained using a piston-type wavemaker. The no-slip boundary condition is imposed on the bottom of the impervious rippled bed. The boundary conditions at the interface between the water and the permeable rippled bed are the continuity of the velocities and the continuity of normal and tangential stresses (Deresiewicz and Skalak, 1963). They are expressed in dimensionless form as (Huang et al., 2003)

$$u_w=n_w u_p \tag{7}$$

$$v_w=n_w v_p \tag{8}$$

$$\left(-p+\frac{2}{\mathrm{Re}}\frac{\partial v}{\partial y}\right)_w=\left(-p+\frac{2}{\mathrm{Re}}\frac{\partial v}{\partial y}\right)_p \tag{9}$$

$$\left(\frac{\partial u}{\partial y}+\frac{\partial v}{\partial x}\right)_w=\left(\frac{\partial u}{\partial y}+\frac{\partial v}{\partial x}\right)_p \tag{10}$$

where the subscript "w" refers to physical variables in the water, while "p" refers to those in the porous media.

The downstream boundary condition used by Huang and Dong (2002) was also applied herein to ensure that at a large distance from the wavemaker, the wave is outgoing without reflection. The velocities, hydrodynamic pressure and surface displacements are set to zero at time $t=0$. Both the governing equations and the boundary conditions, including the kinematic and dynamic free surface boundary conditions (Huang and Dong, 2002), the interface boundary conditions, Eqs. (9) and (10), as well as the downstream boundary conditions, are transformed herein from the physical space (x,y,t) into computational space (ξ,η,t). These transformed equations are then solved numerically.

3. Numerical method

In this study, the finite-analytical method (Chen and Chen, 1982; Chen and Patel, 1987) was applied as in Huang and Dong (2002) to discretize the transformed forms of the unsteady two-dimensional Navier–Stokes equations and the Navier–Stokes type model equations for porous flows. The SIMPLER algorithm developed by Patankar (1980) was used to calculate the coupled velocity and pressure fields. A staggered numerical grid was used. The velocity components u and v are defined at the boundaries of a control volume, while the pressure p is defined at the center. The Marker and Cell method (Harlow and Welch, 1965) and its modified version SUMMAC (Chan and Street, 1970) were combined to calculate the free surface boundary.

The value of each variable at each nodal point was related to the values of the four neighboring nodal points, except at the interface or on the boundaries. To interpret the boundary conditions at the interface, the variable values at the interface must be carefully determined. Accordingly, numerical grid cells were distributed on both sides of the interfaces (see Fig. 2). The values for u_w and u_p on both sides of the interface were determined from Eqs. (7) and (10), in which the unknown value of v was replaced with its value in the previous time step. Since only one equation, Eq. (8), is available to determine v_w and v_p at the interface, the conservation of mass is applied to the cell beneath the interface to determine v_p and then v_w was computed from Eq. (8). The pressure p_w on the upper side of the interface was determined from the flow domain using a three-point extrapolation formula. The pressure p_p on the lower side of the interface was then calculated from p_w using Eq. (9).

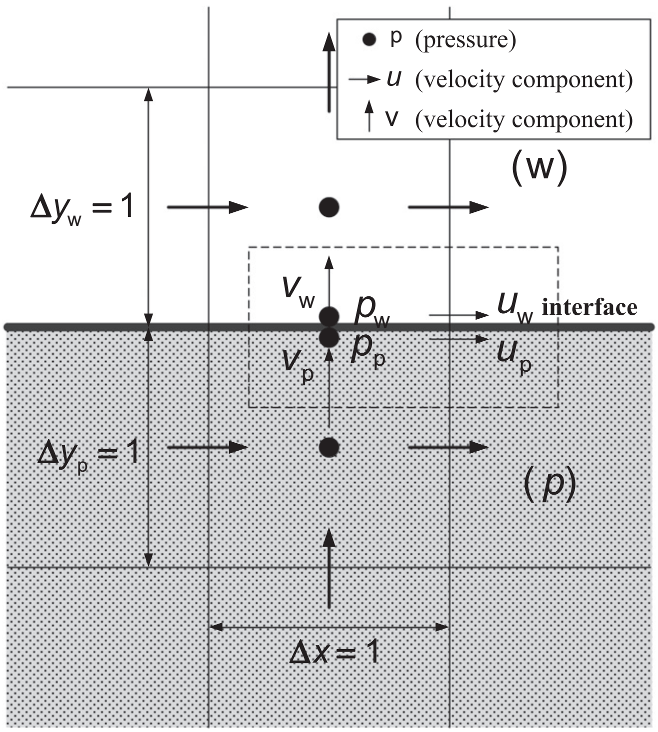

Fig. 2. Physical variables near interface between water region (w) and porous bed (p).

4. Results and discussions

4.1. Verification of the numerical scheme

Before the propagation of water waves over permeable rippled beds can be investigated, the suitability of the proposed model equations for pore flows must be tested. The model equations were employed to simulate the propagation of waves over a permeable bed. Liu et al. (1996) studied this problem both theoretically and experimentally. Both the analytical solutions and the experimental velocity profiles within the bottom boundary layer above the porous bed were available. The analytical solutions also yield the velocity and pressure in the porous bed. Fig. 3 compares the numerical, theoretical and experimental velocity profiles near the interface induced by incident waves of T=1.114 s, H_i=1.074 cm, u_∞=3.567 cm/s, and h_o=24 cm that propagate over a porous bed of n_w=0.39, d_{50}=0.5 mm, $K_p=0.235\times 10^{-9}\,\mathrm{m}^2$, and h_p=33.5 cm, where T and H_i are the period and the height of the incident waves; h_o is the depth of the still water; n_w and h_p are the porosity and the depth of the porous bed, and d_{50} is the mean grain diameter. The permeability coefficient K_p was calculated using Eq. (5). In Fig. 3, $u_\infty = a\omega/\sin h\, kh_o$, and δ denotes the characteristic thickness of the bottom boundary layer, $\delta=\sqrt{\upsilon/\omega}$, where a, ω and k are the amplitude, the angular frequency and the wavenumber of the waves, respectively. The flow velocity in the porous bed is the Darcian velocity. Although in Sections 2 and 3, the symbols u, x, p, t and others, are non-dimensionalized physical variables, in this section and in the figures, for simplicity, these symbols are adopted to represent the original physical variables. Fig. 3 reveals that although both the theoretical and the numerical results match the experimental data, the numerical results are closer to the experimental data. Fig. 4 compares the numerical and theoretical pore pressures at the wave crest under the same conditions as in Fig. 3. In Fig. 4, p_o denotes the pore pressure at the interface. Liu et al. (1996) determined the theoretical pore pressure as

$$p=\rho ga\frac{\cos h\, k(y+h_p)}{\cos h\, kh_o \cos h\, kh_p} \tag{11}$$

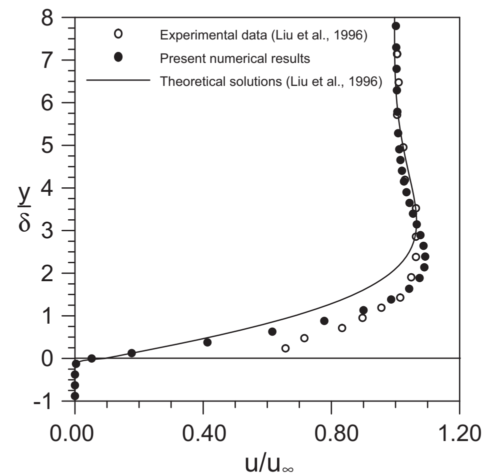

Fig. 3. Comparison of numerical, theoretical, and experimental velocity profiles near bottom boundary layer above the porous bed induced by incident waves of T=1.114 s, H_i=1.074 cm, u_∞=3.567 cm/s and h_o=24 cm propagating over a porous bed of n_w=0.39, d_{50}=0.5 mm, $k_p=0.235\times10^{-9}\,\mathrm{m}^2$ and h_p=33.5 cm.

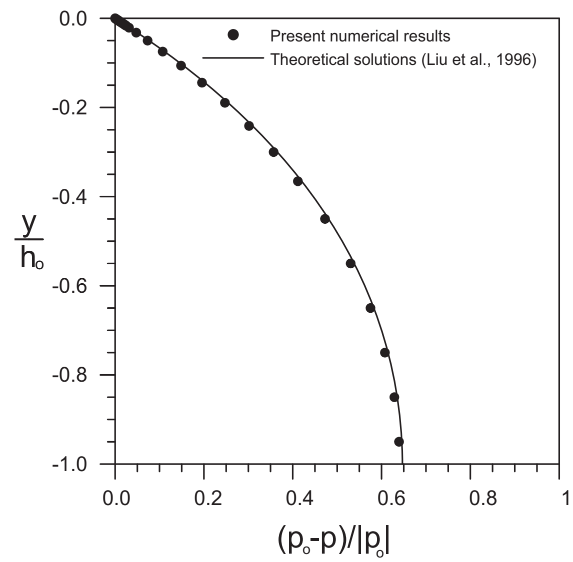

Fig. 4. Comparison of numerical and theoretical pore water pressure induced by propagation of waves over a porous bed under the same conditions as in Fig. 3.

where g is the gravitational acceleration. The numerical pore pressure is exactly the theoretical value. The comparisons in Figs. 3 and 4 show that the porous flow model equations accurately describe the flow in porous structures.

To confirm the accuracy of the proposed numerical scheme, the numerical results for the spatial distributions of wave height on both impermeable and permeable rippled beds were compared with the analytical solutions of Mase et al. (1995). In their work, the incident wave period T=1.31 s, the wave height H_i=3.0 cm, the still water depth h_o=0.313 m, the wavelength L=2.01 m, and the rippled bed had several ripples with a wavelength of λ_s=1.0 m ($k_s=2\pi/\lambda_s$) and a height of a_s=10.0 cm (Fig. 5). The total length of the rippled bed was 10 m. The geometry of the ripples was

$$y_s=\frac{1}{2}a_s\sin(k_s x_s),\;\; s_t\le x_s\le m\lambda \tag{12}$$

where s_t is the beginning of the rippled bed, m is the number of ripples and m=10. The y coordinate of the flat bottom was set to 0.0; hence, the y coordinates of the ripple crest and trough were

+5.0 and −5.0 cm, respectively. The permeable rippled bed had a mean depth of h_p=0.2 m and porosity n_w=0.4. Mase et al. (1995) did not provide the grain size. In this investigation, d_{50} was taken as 1.5 cm. Wave and rippled bed conditions examined by Mase et al. (1995) are presented in Table 1 and denoted as Case Test-I and Case Test-P, with the former representing the impermeable rippled bed and the latter the permeable rippled bed.

Fig. 6 plots the numerical grid distribution in the rippled section of the computational domain. The rippled bed begins at x/h_o=107.85 and ends at x/h_o=139.80. One hundred grid cells are distributed between each pair of successive ripple crests; for clarity, only 20 are shown in Fig. 6. The vertical mesh interval $\Delta y/h_o$ varies from about 0.01 in the near-bed region to 0.034 in the lower region and 0.05 in the upper region of the physical domain. The physical domain (x,y) and the computational domain (ξ,η) are related as

$$x/h_o = \begin{cases} 0.01(\lambda_s/h_o)\xi & \text{in the rippled section} \\ 0.25\xi & \text{outside the rippled section} \end{cases} \tag{13}$$

$$y/h_o = \begin{cases} 0.05\eta & \text{for } y/h_o \geq 0.30 \\ (0.3-y_s/h_o)\eta/30 & \text{for } 0.0 \leq y/h_o \leq 0.3 \\ (y_s/h_o-0.3)\eta/30 & \text{for } -0.3 \leq y/h_o \leq 0.0 \\ 0.034\eta & \text{for } -0.64 \leq y/h_o \leq -0.3 \end{cases} \tag{14}$$

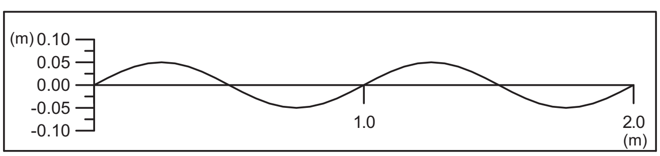

Fig. 5. Geometry of ripples in the Test Case.

Table 1
Numerical conditions.

Wave type	Periodic waves					Solitary wave	
Case	Test-I	Test-P	1	2	3	4	5
h_o (m)	0.313	0.313	0.17	0.17	0.17	0.17	0.17
H_i (cm)	3.0	3.0	6.0	6.0	6.0	2.55	2.55
T (s)	1.31	1.31	1.09	1.09	1.09	–	–
L (m)	2.01	2.01	1.27	1.27	1.27	–	–
U_r	3.96	3.96	19.7	19.7	19.7	–	–
a_s (cm)	10.0	10.0	1.0	1.0	1.0	1.0	1.0
λ_s (cm)	100.0	100.0	5.0	5.0	5.0	5.0	5.0
m	10	10	10	10	10	10	10
h_p/h_o	–	0.64	–	0.5	0.5	–	0.5
n_w	–	0.4	–	0.4	0.521	–	0.4
d_{50} (cm)	–	1.5	–	1.5	2.09	–	1.5
K_p($\times 10^{-7}$ m^2)	–	0.522	–	0.522	3.22	–	0.522
C_f	–	0.39	–	0.39	0.73	–	0.39
Wall type	A	A	B	B	B	B	B

Note: A=ripple form using Eq. (12), B=ripple form using Eq. (15) and $U_r = H_i L^2/h_o^3$.

The increments of ξ and η, $\Delta\xi$ and $\Delta\eta$, are set to 1.0. The independence of the numerical results from the grid was tested using finer grids in both x- and y-directions. A successive over-relaxation factor, between 1.2 and 1.4, was used to accelerate the convergence of the SIMPLER algorithm for pressure.

Fig. 7(a) and (b) compare the numerical and theoretical spatial distributions of wave height on an impermeable and a permeable rippled bed, respectively. The beginning of the rippled bed was set to X=0 m. The factor, f_c, represents the friction coefficient of the permeable bed in the model of Mase et al. (1995). In Fig. 7, the condition of $L/\lambda_s \cong 2.0$ is satisfied, and the variation of the wave heights is remarkable. Fig. 7 demonstrates that the numerically determined wave heights on both impermeable and permeable rippled beds herein agree very well with the analytical solutions determined by Mase et al. (1995). Fig. 7 reveals that when the bottom is permeable, the amplitudes and their variations become small downstream.

4.2. Propagation of regular waves over permeable rippled beds

Following the verification of the accuracy of the numerical method, the propagation of the water waves over a permeable rippled bed is investigated. Table 1 presents the incident waves and the rippled bed conditions. The incident waves are chosen to be either Stokes waves or the solitary waves. Both waves are generated using a piston-type wavemaker in the computational domain. The wave conditions and the geometry of the rippled bed in Table 1 were selected to reproduce the results of Huang and Dong (2002) for an impermeable rippled bed. They explored the propagation of waves over an impermeable rippled bed using the same approach as the present one. Notably, the rippled bed in Cases 1 to 5 is not the same as that used in the test cases. The geometry of the

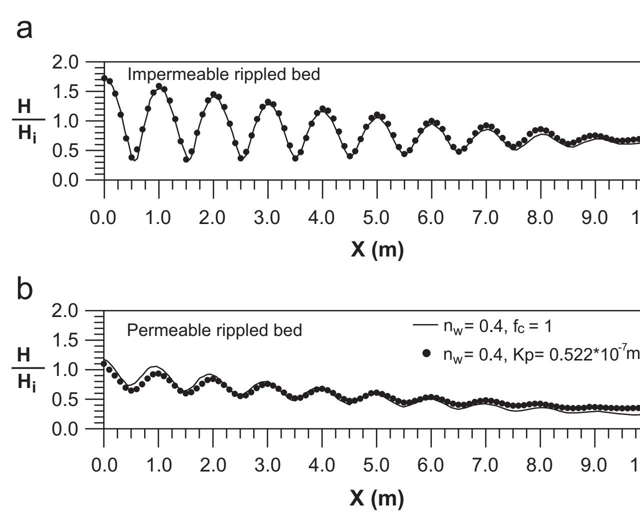

Fig. 7. Spatial distribution of wave heights under resonant condition; (—) analytical solutions (Mase et al., 1995), (●) results obtained using present numerical model.

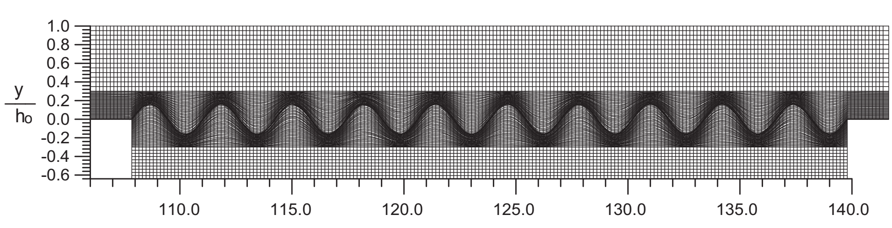

Fig. 6. Numerical grids in rippled section in computational domain.

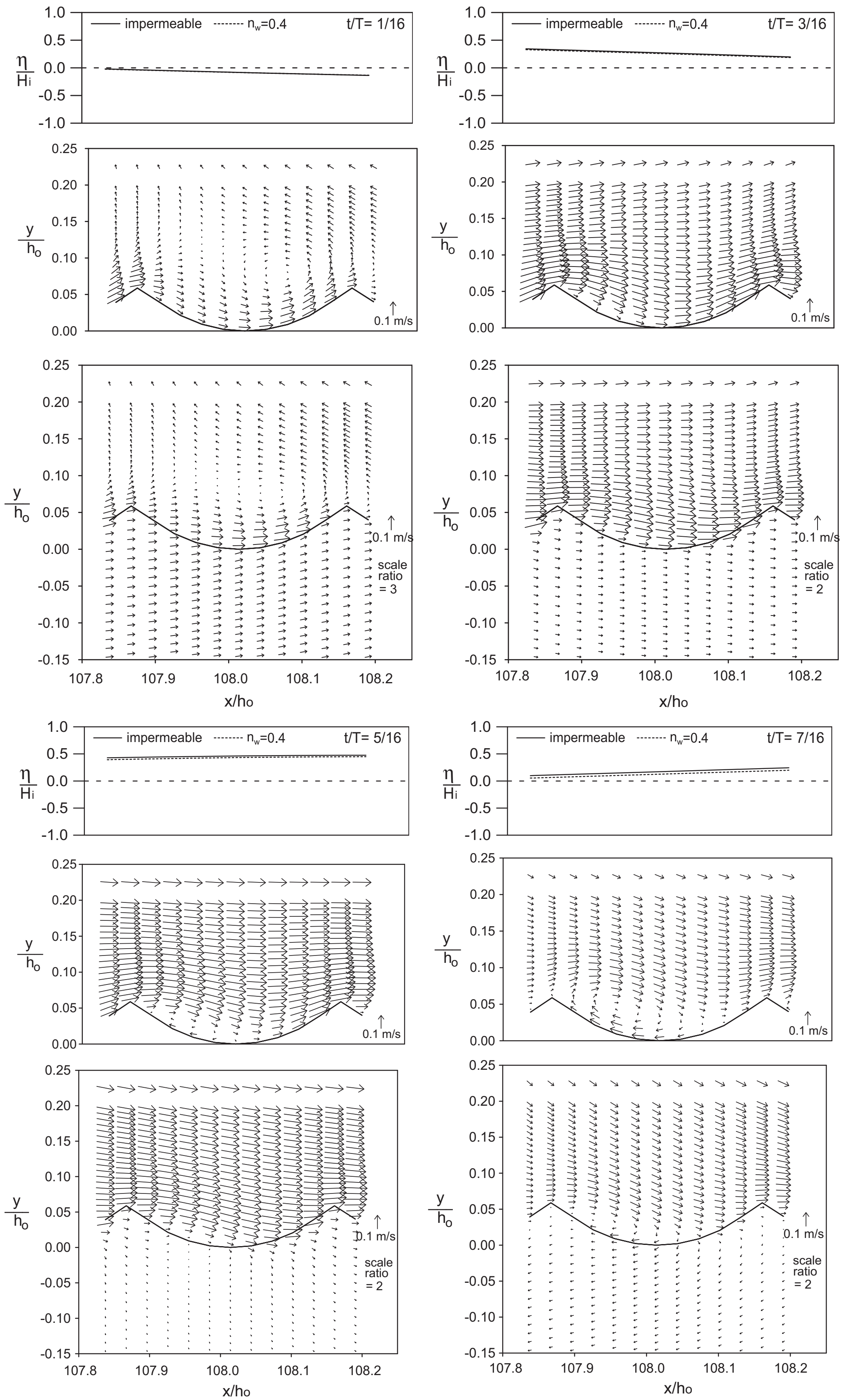

Fig. 8. Variation of free surface elevations and velocity fields within a wave period for impermeable (Case 1) and permeable (Case 2) rippled beds.

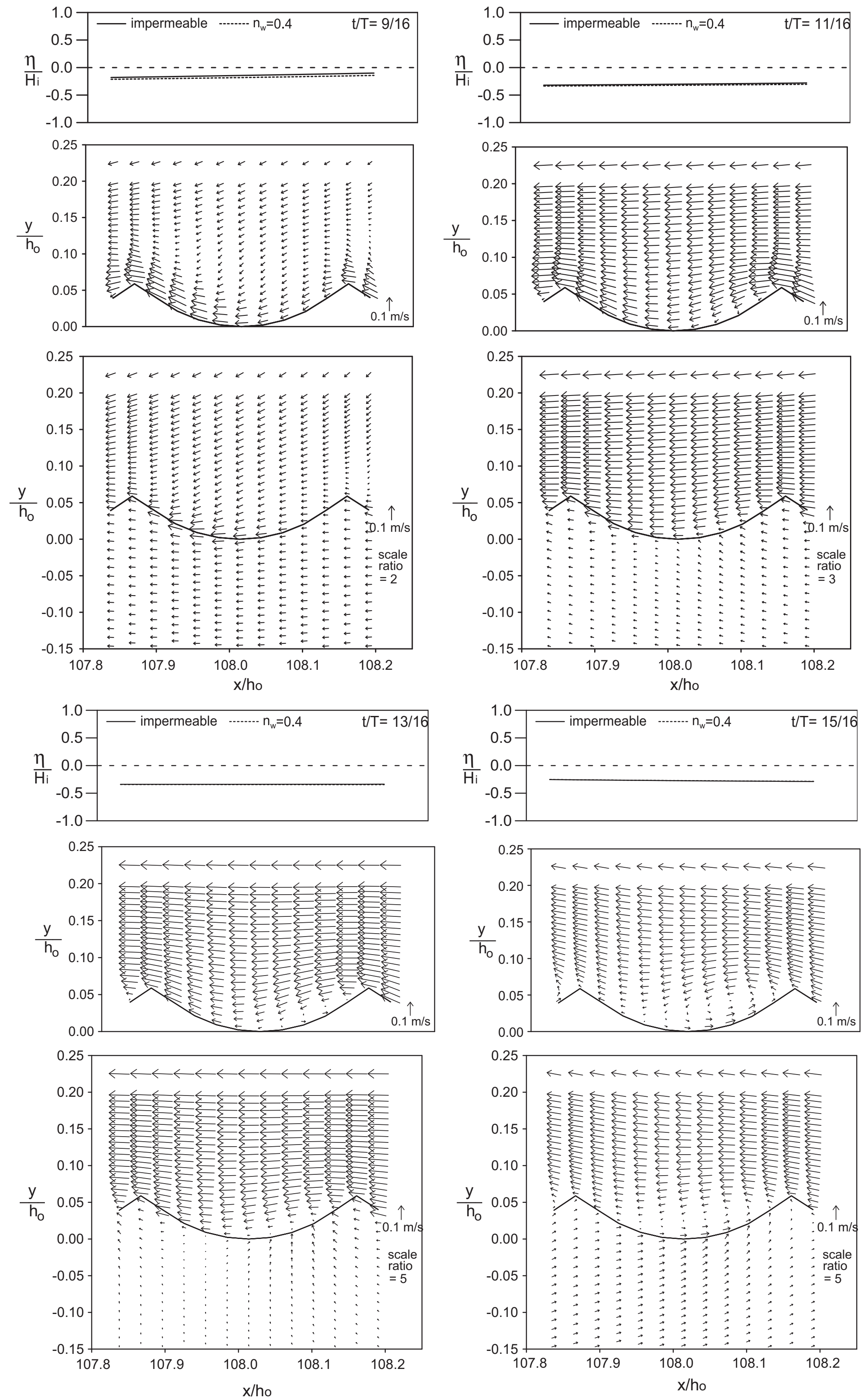

Fig. 8. (*Continued*)

ripples studied in Cases 1 to 5 is given by

$$x_s = \zeta - \frac{1}{2} a_s \sin k_s \zeta \tag{15a}$$

$$y_s = \frac{1}{2} a_s \cos k_s \zeta \tag{15b}$$

The y coordinate of the ripple troughs is set to $y/h_o = 0$.

Fig. 8 plots the variation of the free surface elevations and velocity fields in a single wave period as Stokes waves propagate over a rippled bed in Cases 1 and 2 from Table 1. The accuracy of the numerical flow fields was verified by Huang and Dong (2002), who compared the numerical results of the instantaneous velocity field near rigid ripples with the experimental data of Hwung and Hwang (1993). To visualize the flow field in the rippled porous bed, the velocity of the flow field is enlarged. The scale ratio is indicated in the figure; for example, the scale ratio=3 at $t/T=1/16$. Fig. 8 reveals that when a wave crest propagates over the crest of the rippled bed, such as at $t/T=3/16$, flow separation with reattachment occurs, subsequently forming a clockwise vortex later on the lee side of the ripple crest, at $t/T=5/16$ and 7/16. Conversely, when a wave trough propagates onto the ripple crest, such as at $t/T=11/16$, flow separation occurs and subsequently develops into a counter-clockwise vortex later on the weather side of the ripple crest, at $t/T=13/16$ and 15/16. The dimensions and heights of the oscillating vortices are comparable with the ripple wavelength and markedly exceed the thickness of the Stokes layer.

When the rippled bed is permeable, the water surface elevation becomes slightly less than that above an impermeable bed, because the flow friction in the porous bed dissipates additional wave energy. Since the flow is allowed to penetrate into or through the porous bed, the clockwise vortex forms on the lee side of ripple (at $t/T=7/16$) and the counter-clockwise vortex at the weather side of the ripple (at $t/T=15/16$) become smaller.

Figs. 9 and 10 present the steady Eulerian streaming velocity close to the wall for the flow fields in Fig. 8. The streaming velocity at each fixed location was calculated by taking a time average over 32 instantaneous velocities over a wave period. Figs. 9 and 10 reveal that the counter-clockwise circulating cell is larger than the clockwise circulating cell on the lee side of the ripple crest. This phenomenon is related to the property of Stokes waves that the time interval of the negative surface elevation is longer than those of the positive surface elevation. Since the counter-clockwise vortex on the weather side of the ripple crest was generated when the wave trough propagated over there, more time was available for the vortex on the weather side to develop. Such a steady streaming velocity differs from that obtained in the oscillating flow, in which the sinusoidal flow field causes the two circulating cells to be of equal size. It is believed that once the sediments are mobilized, these circulating cells can keep them in suspension. As presented in Fig. 10, the circulating cells between the successive ripple crests of a permeable rippled bed are smaller than those over an impermeable rippled bed, because the flow can penetrate the porous bed. The steady streaming velocities in Figs. 9 and 10 indicate that the vortices on the lee and weather sides of the ripples will scour the bottom and keep the sediments in suspension.

To obtain more information on the possible transport of sediment around the rippled bed, the trajectories of the fluid particles whose initial locations were close to the bed are determined. Since the specific weight of the fluid particles differs from that of sands, the trajectories of the fluid particles are not identical to those of the sand particles. However, the former may provide insight into the transport of sediment near the wall. Fig. 11 depicts the initial positions of ten marked fluid particles between two successive ripple crests. These particles are released at the same time when the waves reach the steady state and are traced over three wave periods to determine their trajectories.

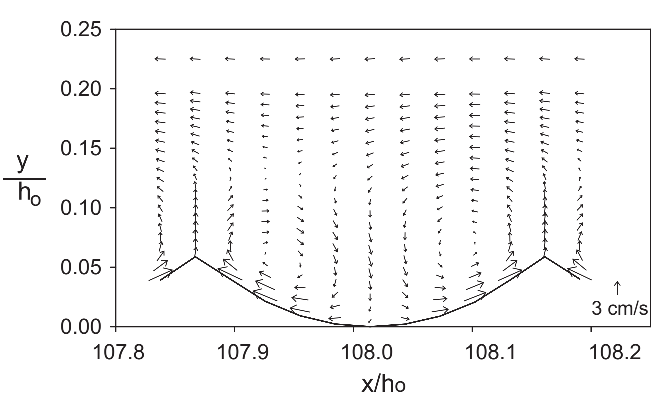

Fig. 9. Steady Eulerian streaming velocity near the wall for flow field in Case 1.

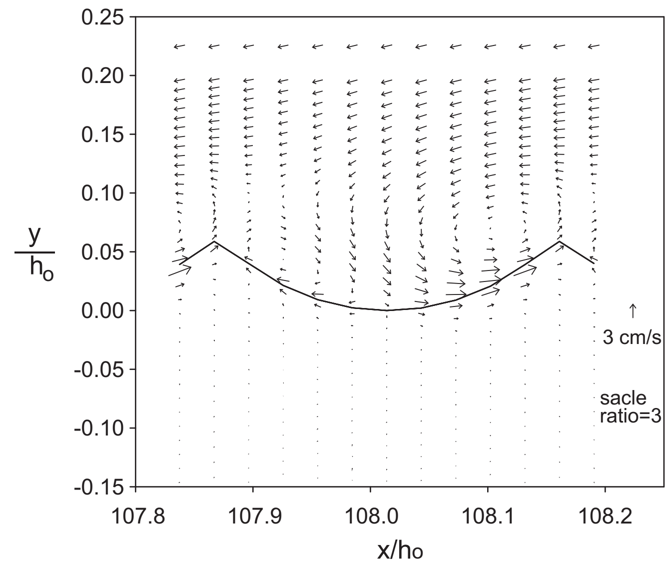

Fig. 10. Steady Eulerian streaming velocity near the wall for flow field in Case 2.

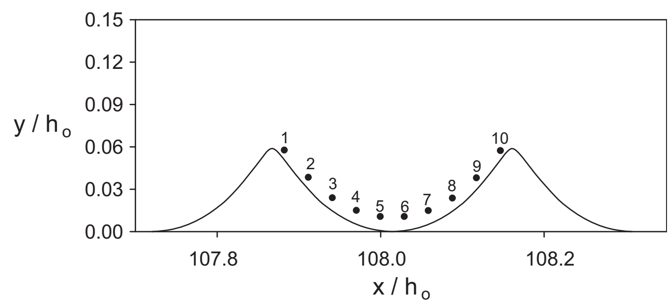

Fig. 11. Initial locations of marked fluid particles with traced trajectories.

Fig. 12(a)–(h) display the trajectories of the first, second, fourth, fifth, sixth, seventh, eighth and tenth marked particles over three wave periods. The "e" in Fig. 12 marks the end of trajectories. The trajectories of the first and second marked particles on an impermeable rippled bed (Case 1) initially move back and forth around the ripple crest with increasing vertical distance from the ripple wall; then, after one or two wave periods, they are lifted up. The first and second particles seem to shift offshore. The fourth particle initially moves in the wave direction toward the next ripple crest; in the second and third wave periods, it was lifted up and transported toward the next ripple crest. The fifth, sixth and seventh particles move initially in the wave direction toward the neighboring ripple crest, and then back and forth around this ripple crest. During the first wave period, the eighth and tenth particles move in the wave direction toward the next ripple crest, and were then lifted up and transported to the next ripple crest, where they again moved back and forth.

Notably, of the eight particle trajectories displayed in Fig. 12, five shift onshore and three shift offshore within three wave

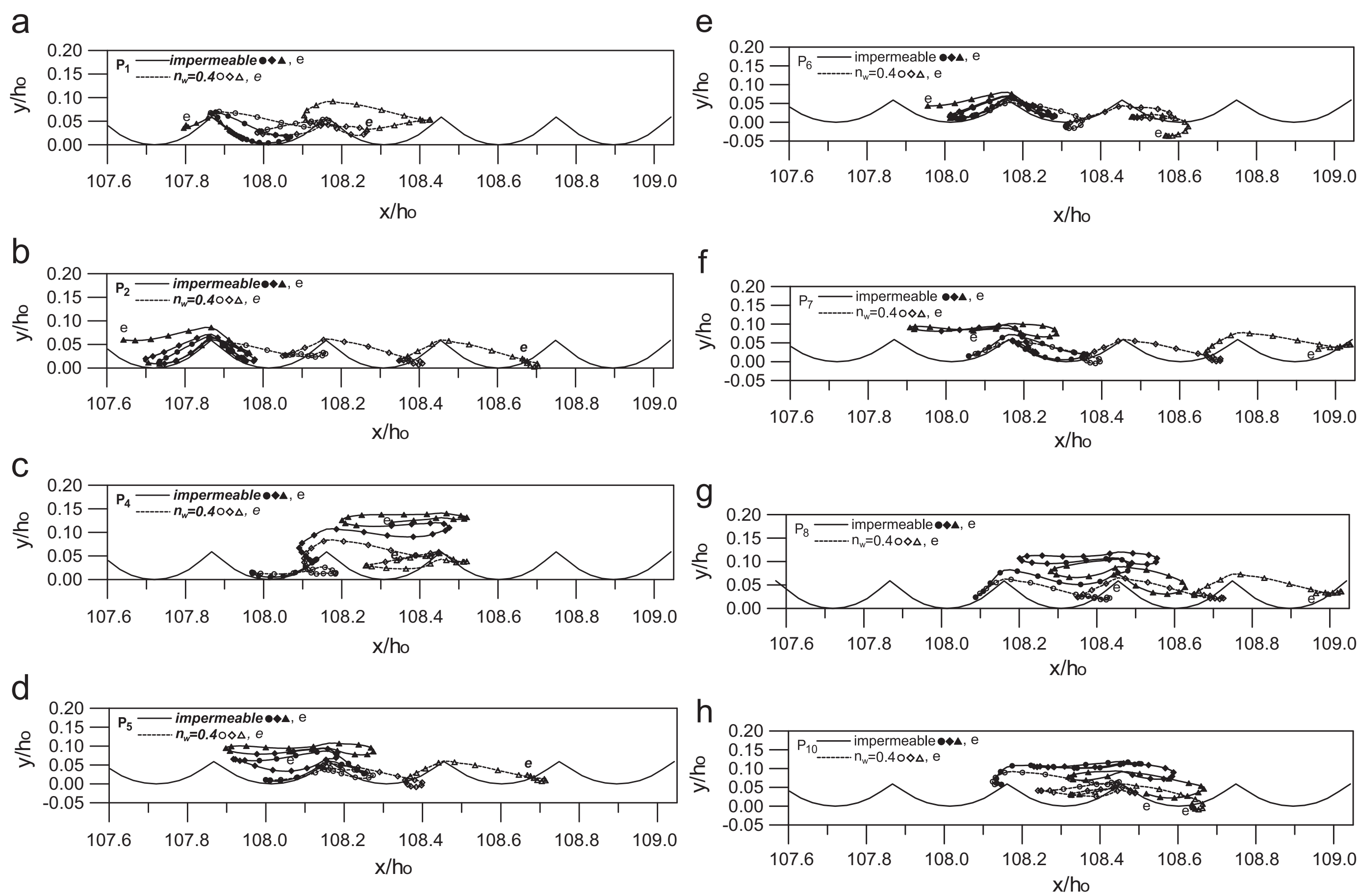

Fig. 12. Trajectories of marked fluid particles over three wave periods for flow fields in Case 1 and Case 2; (●,○) first wave period, (◆,◇) second wave period, and (▲,△) third wave period.

periods. However, over the permeable rippled bed, as also displayed in Fig. 12, all of the particles shift onshore with a much larger displacement than that over the impermeable bed. The reasons for this difference are identified by examining the steady Eulerian streaming velocity in both cases, as shown in Figs. 9 and 10. In the permeable case, the clockwise circulating cell is much smaller than the counter-clockwise circulating cell. Accordingly, the negative (offshore) streaming velocity is much lower than the positive (onshore) streaming velocity near the porous bed. Therefore, the back and forth motion in the impermeable case ceases to dominate the motion of the particles near the porous bed. Most of the back and forth motion occurs on the weather side of the ripple crest because the strongly circulating cell is there. Other than on the weather side of the ripple crest, the particle moves rather straightforwardly in the wave direction.

Fig. 13 displays the steady Eulerian streaming velocity in Case 3, in which the porosity is 0.521, increased from $n_w = 0.4$ in Case 2. The pattern of the circulating cells is approximately the same as that shown in Fig. 11.

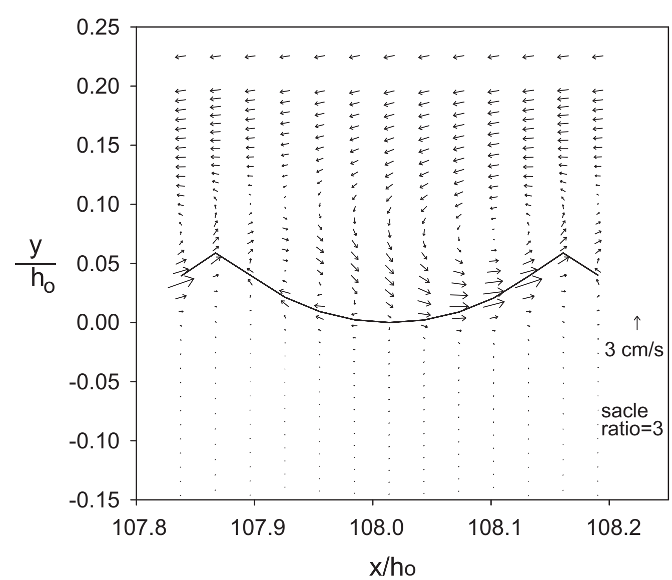

Fig. 13. Steady Eulerian streaming velocity near the wall for flow field in Case 3.

4.3. Propagation of a solitary wave over permeable rippled beds

This section discusses the propagation of a solitary wave over an impermeable or a permeable rippled bed. A solitary wave is frequently used to represent certain characteristics of tsunamis, storm surges, and other long free surface waves. The boundary layer that is induced by a solitary wave propagating over impermeable and permeable flat beds has attracted considerable attention recently (e.g., Huang and Dong, 2001; Liu and Orfila, 2004; Liu et al., 2007; Huang et al., 2008). One of their main findings is that flow separation within the boundary layer occurs in the rear part of the wave profile. This reversed flow is generated by an adverse pressure gradient, which can be recognized from the wave profile, because the pressure fields beneath a solitary wave are nearly hydrostatic (Huang and Dong, 2001). This characteristic persists

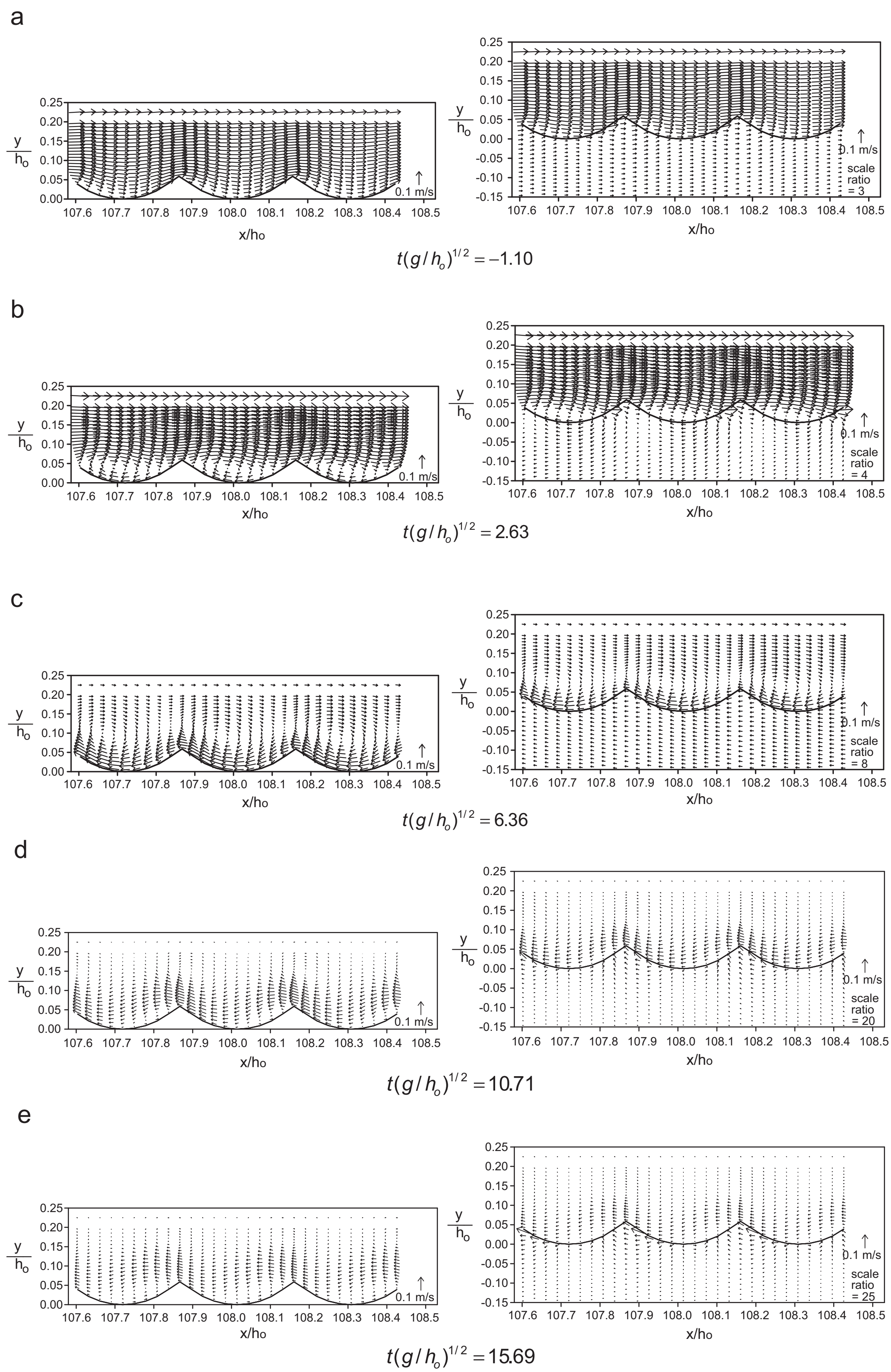

Fig. 14. Instantaneous velocity fields over impermeable (Case 4) and permeable rippled beds (Case 5) induced by a solitary wave of $H_i/h_o = 0.15$ at various times.

even when the bed is permeable (Huang et al., 2008). This information should be considered as more detailed flow behaviors near the rippled bed are to be investigated.

Fig. 14(a)–(e) plot the variation in the flow fields close to impermeable (Case 4) and permeable rippled beds (Case 5), while Fig. 15 plots the instantaneous velocity fields over the whole rippled bed at two instants, induced by a solitary wave of $H_i/h_o=0.15$. In these figures, the time is normalized using $t(g/h_o)^{1/2}$ and set to zero when the wave crest reaches the beginning of the wavy wall, such as at $x/h_o=106.5$. Notably, when the wave crest propagates onto the impermeable ripple section, $t(g/h_o)^{1/2}=-1.10$, flow separation with reattachment occurred on the lee side of each ripple crest. The flow separation gradually develops into a clockwise vortex that covers the entire region between two successive ripple crests, $t(g/h_o)^{1/2}=2.63$. The size of the vortex declines in the wave propagation direction (Fig. 15). The wall effect lifts the generated vortices, $t(g/h_o)^{1/2}=6.36$, and induces a secondary counter-clockwise vortex on the weather side of the ripple crest, $t(g/h_o)^{1/2}=10.71$. The strengths and dimensions of the secondary vortices are much smaller than those of the primary vortices. However, these periodically arranged vortices establish a current in the direction opposite to the wave propagation, $t(g/h_o)^{1/2}=15.69$. This current flows above the ripples and may have an important role in sediment transport because when the primary vortices lift the sands into a suspension, this current may carry the sands away.

When the rippled bed is permeable, the same flow as described above occurs, but the clockwise vortex is smaller than when it is impermeable, as displayed in Fig. 14(b), because the flow could pass through the porous wall, reducing the velocity gradient near the wall. This drop in the velocity gradient in turn reduces the strength of the vorticity. Subsequently, the secondary vortices on the weather side of the ripple crests, induced by the primary vortex, are smaller, as shown in Fig. 14(d). The current above the porous ripples is also weaker.

Fig. 16 plots the trajectories of fluid particles P_1, P_2, P_5, P_6, P_7, P_8, P_9 and P_{10} to provide more information about the characteristics of the flow near the rippled bed. The initial locations of the marked fluid particles are the same as those in Fig. 11, and these particles are released when the wavemaker starts to move. The numbers on the trajectories specify the time order. The "0" time order applies when the wave crest reaches the beginning of the rippled bed. The time interval between two successive numbers is $4(g/h_o)^{-1/2}$. The location of the particles at the successive times is indicated, but only the first two positions are numbered. The information in Fig. 16 is consistent with Figs. 14 and 15, and the fluid particles near the impermeable rippled bed are raised by the primary vortices and are transported by the induced current in the direction that is opposite to that of the wave, indicating that under a solitary wave the sediment may be transported in the direction opposite to that of the wave propagation. This situation differs from the case of periodic waves, in which most of the sediment is transported in the direction of the waves.

The trajectories of fluid particles above the permeable rippled bed are similar to those on the impermeable rippled bed. As stated earlier in reference to Fig. 16, both the primary and the secondary vortices, and the current above the porous ripples, are smaller than those on the rigid ripples. Hence, most of the particles shown in Fig. 16 exhibit a smaller final horizontal displacement. Notably, although all of the fluid particles on the impermeable rippled bed eventually move in the opposite direction of waves, some particles on the porous rippled bed, such as P_5, P_8 and P_9, do move in the direction of the wave.

5. Conclusions

In this work, the unsteady two-dimensional Navier–Stokes equations and Navier–Stokes type model equations for porous flow were solved numerically to investigate the flow fields near permeable and impermeable rippled bed induced by water waves. The boundary-fitted coordinate system was adopted herein. After the accuracy of the numerical scheme was verified, the viscous flow

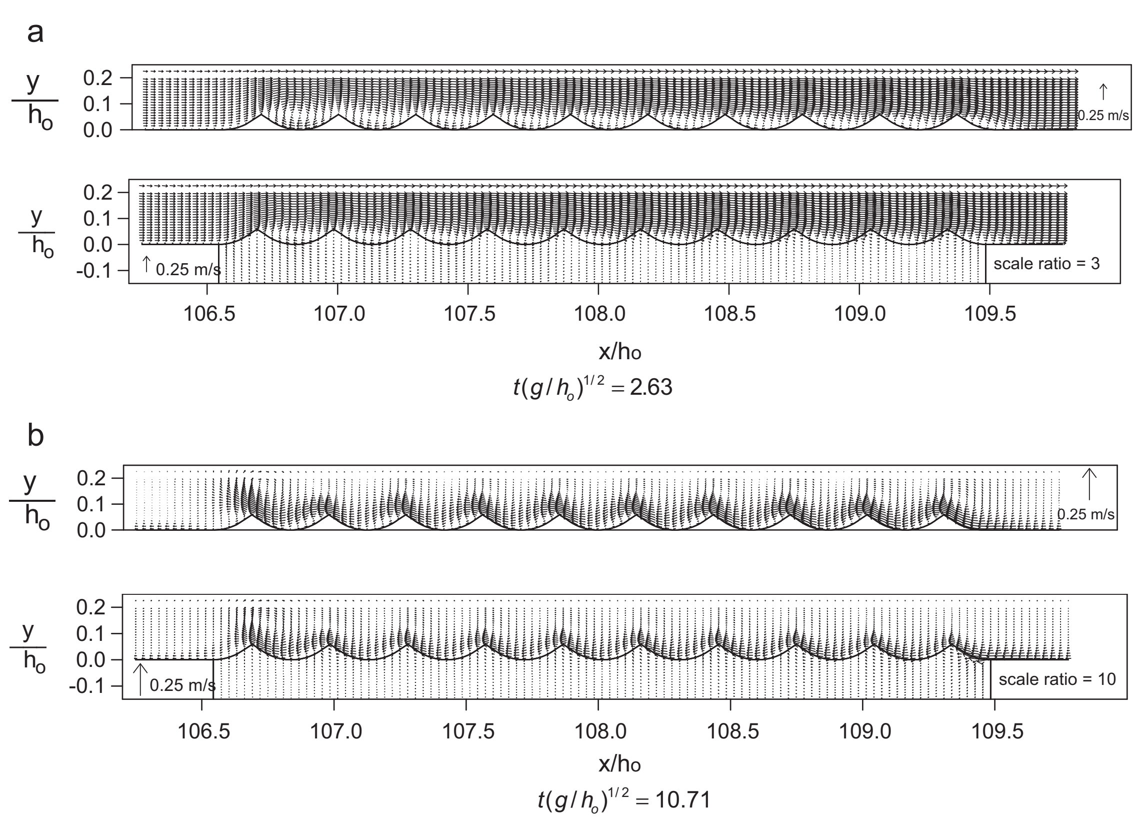

Fig. 15. Instantaneous velocity fields over all impermeable and permeable ripples, induced by a solitary wave of $H_i/h_o=0.15$.

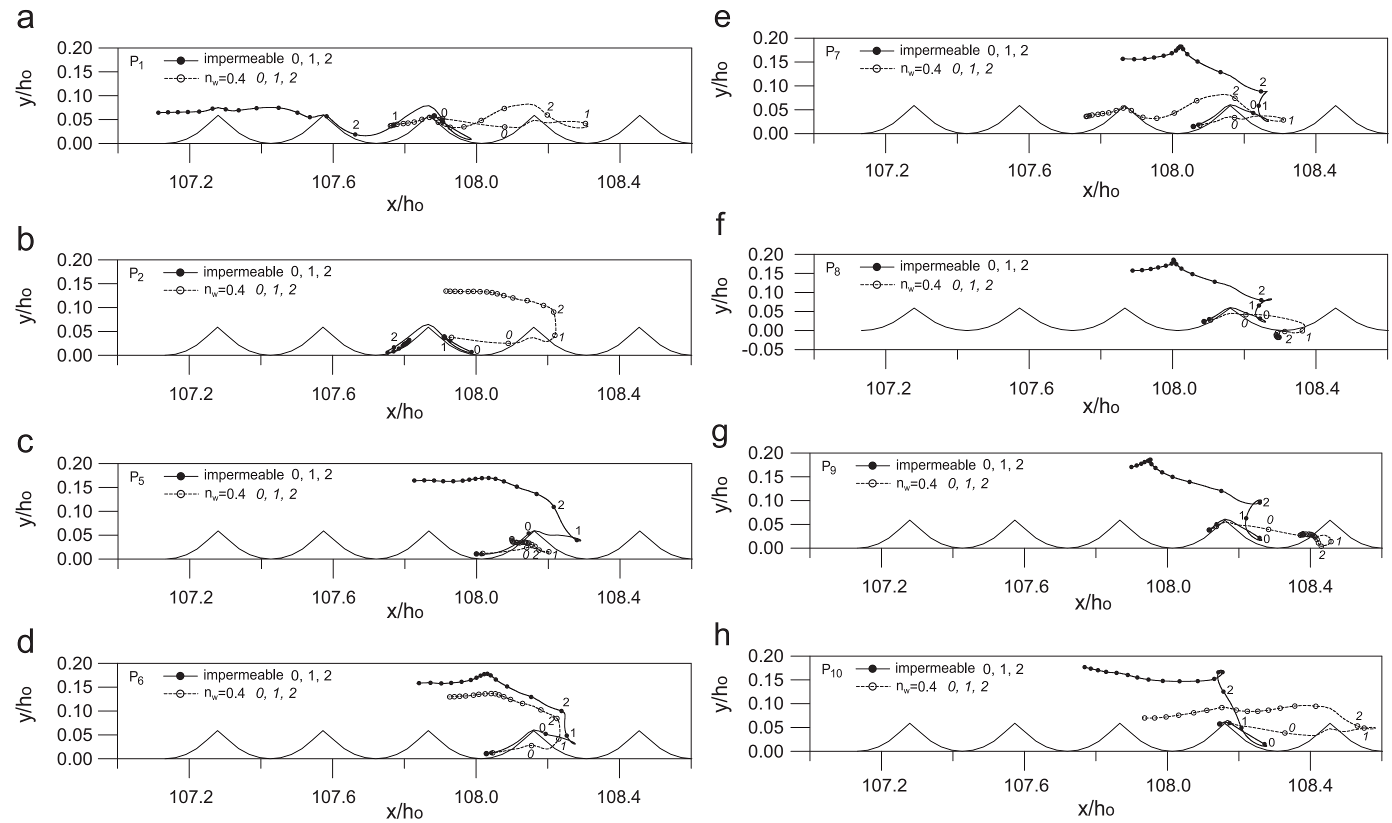

Fig. 16. Trajectories of marked fluid particles in flow fields in Fig. 15.

fields and the associated fluid particle trajectory close to the impermeable and permeable beds were determined. The numerical results support the following conclusions.

1. The propagation of periodic waves propagates over rigid rippled bed produces a clockwise vortex on the lee side of the ripple crest, and a counter-clockwise vortex on the weather side. When the incident waves are Stokes waves, the counter-clockwise circulating cell is larger than the clockwise one. This fact is related to the property of the incident Stokes waves.
2. When the rippled bed is permeable, the water surface elevation becomes slightly lower than that above the impermeable bed, because the flow friction in the porous bed dissipates additional wave energy. The vortices that are generated on both the weather and the lee sides of the porous ripples are also smaller, because the flow is allowed to penetrate into or through the porous bed.
3. In the case of periodic water waves, fluid particles on the impermeable rippled bed initially move back and forth around the ripple crest with increasing vertical distance from the ripple wall. After one or two wave periods they are lifted up and shifted towards the next ripple crest.
4. All of the marked particles on the permeable rippled bed shift onshore with a much larger displacement than on the impermeable bed. The motion of the particles is not predominantly back and forth, except on the weather side of the ripple crest.
5. The propagation of a solitary wave over a ripple section generates a clockwise vortex that covers the region between each pair of successive ripple crests. The generated vortices move upward and induce secondary counter-clockwise vortices on the weather side of each ripple crest. The periodically arranged vortices seem to induce a current in the direction opposite to that of the wave propagation.
6. When the rippled bed is permeable, the same flow as described above occurs, but the clockwise vortex is smaller than in the impermeable case. Subsequently, the secondary vortices on the weather side of the ripple crests are smaller and the current above the porous ripples is also smaller.
7. Under the action of a solitary wave, the fluid particles close to the rippled bed are lifted up by the primary vortices and transported by the induced current in the direction opposite to that of the solitary wave. The trajectories of fluid particles above the permeable rippled bed are similar to those on the impermeable bed. Although all of the fluid particles on the impermeable rippled bed eventually move in the direction opposite to that of the solitary wave, some particles on the permeable rippled bed do move in the direction of the wave.

Acknowledgements

This research was financially supported by the National Cheng Kung University under Grant no. A0060. The authors are grateful to the editor and two anonymous reviewers for their valuable comments and suggestions.

References

Arbhabhiramar, A.M., Dinoy, A.A., 1973. Friction factor and Reynolds number in porous media flow. Journal of Hydraulics Division 99, 901–911.

Barr, B.C., Sinn, D.N., Pierro, T., Winters, K.B., 2004. Numerical simulation of turbulent, oscillatory flow over sand ripples. Journal of Geophysical Research, Oceans 109, C09009. doi:10.1029/2002JC001709.

Berkhoff, J.C.W., 1972. Computation of combined refraction-diffraction. In: Proceedings of the 13th international conference on coastal engineering, ASCE, Vancouver, pp. 471–490.

Blondeaux, P., 1990. Sand ripples under sea waves, Part 1. Ripple formation. Journal of Fluid Mechanics 218, 1–17.

Blondeaux, P., Vittori, G., 1991. Vorticity dynamics in an oscillatory flow over a rippled bed. Journal of Fluid Mechanics 226, 257–289.

Chamberlain, P.G., Porter, D., 1995. The modified mild-slope equation. Journal of Fluid Mechanics 291, 393–407.

Chan, R.K.C., Street, R.L., 1970. A computer study of finite-amplitude water waves. Journal of Computational Physics 6, 68–94.
Chen, C.J., Chen, H.C., 1982. The finite-analytic method. IIHR Report 232-IV, Iowa Institute of Hydraulic Research, The University of Iowa, Iowa City.
Chen, H.C., Patel, V.C., 1987. Laminar flow at the trailing edge of a flat plate. AIAA Journal 25, 920–928.
Cheng, Y.Z., Jiang, C.B., Wang, Y.Y., 2009. A coupled numerical model of wave interaction with porous medium. Ocean Engineering 36, 952–959.
Davies, A.G., Heathershaw, A.D., 1984. Surface-wave propagation over sinusoidally varying topography. Journal of Fluid Mechanics 144, 419–443.
Davies, A.G., Villaret, C., 1999. Eulerian drift induced by progressive waves above rippled and very rough beds. Journal of Geophysical Research 104 (C1), 1465–1488.
Deresiewicz, H., Skalak, R., 1963. On uniqueness in dynamic poroelasticity. Bulletin of the Seismological Society of America 53, 783–788.
Dong, C.M., Huang, C.J., 2004. Generation and propagation of water waves in a two-dimensional numerical viscous wave flume. Journal of Waterway, Port, Coastal and Ocean Engineering 130, 1–11.
Hara, T., Mei, C.C., 1990a. Oscillating flows over periodic ripples. Journal of Fluid Mechanics 211, 183–209.
Hara, T., Mei, C.C., 1990b. Centrifugal instability of an oscillatory flow over periodic ripples. Journal of Fluid Mechanics 217, 1–32.
Harlow, F.H., Welch, J.E., 1965. Numerical calculation of time-dependent viscous incompressible flow of fluid with free surface. Physics of Fluids 8, 2182–2189.
Horikawa, K., Watanabe, A., 1968. Laboratory study on oscillatory boundary layer. In: Proceedings of the 11th international conference on coastal engineering, ASCE, London, pp. 467–486.
Hsiao, S.C., Liu, P.L.F., 2003. Oscillatory flows over a permeable wavy boundary. The Chinese Journal of Mechanics-Series A 19, 279–297.
Hsu, T.J., Sakakiyama, T., Liu, P.L.F., 2002. A numerical model for wave motions and turbulence flows in front of a composite breakwater. Coastal Engineering 46, 25–50.
Huang, C.J., Zhang, E.C., Lee, J.F., 1998. Numerical simulation of nonlinear viscous wavefields generated by a piston-type wavemaker. Journal of Engineering Mechanics 124, 1110–1120.
Huang, C.J., Dong, C.M., 2001. On the interaction of a solitary wave and a submerged dike. Coastal Engineering 43, 265–286.
Huang, C.J., Dong, C.M., 2002. Propagation of water waves over rigid rippled beds. Journal of Waterway, Port, Coastal and Ocean Engineering 128, 190–201.
Huang, C.J., Chang, H.H., Hwung, H.H., 2003. Structural permeability effects on the interactions of a solitary wave and a submerged breakwater. Coastal Engineering 49, 1–24.
Huang, C.J., Shen, M.L., Chang, H.H., 2008. Propagation of a solitary wave over rigid porous beds. Ocean Engineering 35, 1194–1202.
Hwung, H.H., Hwang, K.S., 1993. Flow structures over a wavy boundary in wave motion. In: Proceedings of the 9th symposium on turbulent shear flows, Kyoto, pp. 306.1–306.4.
Johnson, I.G., Carlsen, N.A., 1976. Experimental and theoretical investigations in an oscillatory turbulent boundary layer. Journal of Hydraulic Research 14, 45–59.
Kirby, J.T., 1986. A general wave equation for waves over rippled beds. Journal of Fluid Mechanics 162, 171–186.
Lara, J.L., Garcia, N., Losada, I.J., 2006. RANS modelling applied to random wave interaction with submerged permeable structures. Coastal Engineering 53, 395–417.
Liu, P.L.F., Davis, M.H., Downing, S., 1996. Wave-induced boundary layer flows above and in a permeable bed. Journal of Fluid Mechanics 325, 195–218.
Liu, P.L.F., Orfila, A., 2004. Viscous effects on transient long-wave propagation. Journal of Fluid Mechanics 520, 83–92.
Liu, P.L F., Park, Y.S., Cowen, E.A., 2007. Boundary layer flow and bed shear stress under a solitary wave. Journal of Fluid Mechanics 574, 449–463.
Liu, L.F., Lin, P., Chang, K.A., Sakakiyama, T., 1999. Numerical modeling of wave interaction with porous structures. Journal of Waterway, Port, Coastal and Ocean Engineering 125, 322–330.
Longuet-Higgins, M.H., 1953. Mass transport in water waves. Philosophical Transactions of Royaol Society of London A245, 535–581.
Losada, I.J., Lara, J.L., Guanche, R., Gonzalez-Ondina, J.M., 2008. Numerical analysis of wave overtopping of rubble mound breakwaters. Coastal Engineering 55, 47–62.
Lyne, W.H., 1971. Unsteady viscous flow over a wavy wall. Journal of Fluid Mechanics 50, 33–48.
Malarkey, J., Davies, A.G., 2004. An eddy viscosity formulation for oscillatory flow over vortex ripples. Journals of Geophysical Research, Oceans 109, C12016. doi:10.1029/2003JC002086.
Marin, F., 2004. Eddy viscosity and Eulerian drift over rippled beds in waves. Coastal Engineering 50, 139–159.
Martin, C.S., 1970. Effect of a porous sand bed on incipient sediment motion. Water Resources Research 6, 1162–1174.
Mase, H., Takeba, K., Oki, S., 1995. Wave equation over permeable rippled bed and analysis of Bragg scattering of surface gravity waves. Journal of Hydraulic Research 33, 789–812.
McDougal, W.G., 1993. State of the Art Practice in Coastal Engineering. Lecture Notes, National Cheng Kung University, Taiwan, pp. 10.25–10.28.
Patankar, S.V., 1980. Numerical heat transfer and fluid flow. McGraw-Hill, New York.
Ranasoma, K.I.M., Sleath, J.F.A., 1992. Velocity measurements close to the rippled beds. In: Proceedings of the 23rd international conference on coastal engineering, ASCE, Venice, pp. 2383–2396.
Ridler, E.L., Sleath, J.F.A., 2000. Effect of bed roughness on time-mean drift induced by waves. Journal of Waterway, Port, Coastal and Ocean Engineering 126, 23–29.
Sato, S., Shimosako, K., Watanabe, A., 1987. Measurements of oscillatory boundary layer flows above ripples with a laser-Doppler velocimeter. Coastal Engineering in Japan 30, 89–98.
Shao, S., 2010. Incompressible SPH flow model for wave interactions with porous media. Coastal Engineering 57, 304–316.
Silva, R., Salles, P., Palacio, A., 2002. Linear waves propagating over a rapidly varying finite porous bed. Coastal Engineering 44, 239–260.
Sollitt, C.K., Cross, R.H., 1972. Wave transmission through permeable break-waters. In: Proceedings of the 13th international conference on coastal engineering, ASCE, pp. 1872–1864.
Thompson, J.F., Warsi, Z.U.A., Matson, C.W., 1985. Numerical grid generation. Elsevier, New York.
van Gent, M.R.A., 1995. Wave interaction with permeable coastal structures. Ph.D. Thesis, Delft University of Technology, Delft, The Netherlands.